JOURNAL OF AIRCRAFT
Vol. 45, No. 6, November–December 2008

# Flight Control System Design for Inherent Damage Tolerance

Ronald A. Hess* and Gianluca Cama†
*University of California, Davis, Davis, California 95616*

DOI: 10.2514/1.36639

**An approach to the design of damage-tolerant flight control systems is discussed. The design philosophy is based upon a frequency-domain interpretation of pseudo-sliding-mode control. The methodology uses asymptotic observers to accommodate the effects of actuator dynamics in the vehicle being controlled. The technique is attractive in that no failure identification or system reconfiguration/adaptation is required after damage. The vehicle model chosen for study is a simple lateral-directional model of an F-18 fighter. The choice of this model was predicated on the ready availability of linearized models of the aircraft at a variety of flight conditions and the fact that an existing robust design was available for performance comparisons. After a brief introduction to the design technique, the F-18 design is presented. It is shown that controller scheduling for different flight conditions can be accomplished through the observers alone. A model of the human pilot is included to assess performance and handling qualities in a computer simulation of the resulting pilot/vehicle system. Robustness to modeled damage/failure is demonstrated, including a comparison with an existing robust design applied to the same vehicle model.**

## I. Introduction

RESEARCH into control system designs that can allow an aircraft to withstand significant damage or system failures without loss of control is of continuing interest to the aviation community. Couched under a variety of names such as refuse-to-crash, self-healing, reconfigurable, adaptive, etc., these control system technologies all have the common goal of providing a robust flight control design [1,2]. The methodologies that have been proposed and developed typically require 1) detection/identification of damage or failures and 2) system adaptation or reconfiguration in response to these events. The systems that can fulfill these requirements are complex and obviously require finite time to bring the vehicle into a stabilizable state after damage or failure. In certain applications, such as the control of high-performance military aircraft that are open-loop unstable, this time interval can be critical. The research to be described herein has the potential of obviating the necessity of identification and adaptation/reconfiguration in the presence of damage or failure. As such, it may provide a viable alternative to the more complex systems that have been proposed.

The current study has been preceded in the literature by a series of related applications relying upon computer simulation to validate the methodology (e.g., [3–11]). All of this work stems from the research initially reported in [10]. As will be seen, the methodology is based upon sliding-mode control system design techniques [12]. Because a number of previous studies that employ the design technique to be described have appeared in the literature, it is important to outline the contributions of this study. These can be identified as the application of the technique to multiple flight conditions requiring only observer scheduling, evaluation of predicted handling qualities across the flight conditions, description of a simple technique for reducing the likelihood of pilot-induced oscillations after damaged has occurred, and performance comparison with an existing robust design using the same aircraft model and flight conditions.

Presented as Paper 7432 at the AIAA Guidance, Navigation, and Control Conference, 17–20 August 2008, Honolulu, HI. Received 13 January 2008; revision received 12 June 2008; accepted for publication 17 June 2008. 

*Professor, Department of Mechanical and Aeronautical Engineering. Associate Fellow AIAA.

†Graduate Student, Department of Mechanical and Aeronautical Engineering; currently Early Stage Researcher, Ph.D. Student, University of Magdeburg, Germany.

## II. Vehicle Model

The vehicle selected for study is a linearized model of the lateral/directional dynamics of an F-18 fighter aircraft, as reported in [13]. The vehicle is shown in Fig. 1. The model presented in [13] was linearized about 31 flight conditions, as shown in Table 1. For the present study, attention will be focused upon the 19 flight conditions above Mach 0.5, called out by the footnote in Table 1. These represent flight conditions with dynamic pressure exceeding approximately 200 $\text{lbf}/\text{ft}^2$ (with concomitant angles of attack less than 4.26 deg). The reasons for this limitation will be discussed in a later section. Referring to Fig. 1, the control effectors for the vehicle are 1) ailerons $\delta_{\text{ail}}$, 2) (differential) horizontal tail $\delta_{\text{ht}}$, 3) rudder $\delta_{\text{rud}}$, 4) leading-edge flaps $\delta_{\text{lef}}$, and 5) trailing-edge flaps $\delta_{\text{tef}}$. The lateral-directional dynamics are described by a model involving four states: body-axis roll rate $p$, yaw rate $r$, sideslip angle $\beta$, and roll attitude $\phi$. Amplitude- and rate-limited second-order actuator dynamics are included for each of the four effectors. A state-space description for the vehicle at the design flight condition considered here (flight condition 11 in Table 1) and the actuator models is given in Appendix A. The state-space model is given by

$$\dot{\mathbf{x}} = \mathbf{A}\mathbf{x} + \mathbf{B}\mathbf{u} \tag{1}$$

where

$$\mathbf{x} = [p(\text{deg}/\text{s}),\ r(\text{deg}/\text{s}),\ \beta(\text{deg}),\ \phi(\text{deg})]^T$$

and

$$\mathbf{u} = [\delta_{\text{ail}}(\text{deg}),\ \delta_{\text{ht}}(\text{deg}),\ \delta_{\text{rud}}(\text{deg}),\ \delta_{\text{lef}}(\text{deg}),\ \delta_{\text{tef}}(\text{deg})]^T$$

## III. Sliding-Mode Design Technique

The sliding-mode control (SMC) design technique to be used here has been adequately discussed in [3–11] and will only be briefly described here. The design follows a series of steps as follows:

1) A vehicle model is obtained.

2) A control structure is identified. Here, a square control structure is used with command response variables of vehicle roll rate and sideslip. If redundant control effectors are in evidence, a control distribution matrix must be determined. The design requires that no transmission zeros lie in the right-half plane and any uncontrollable

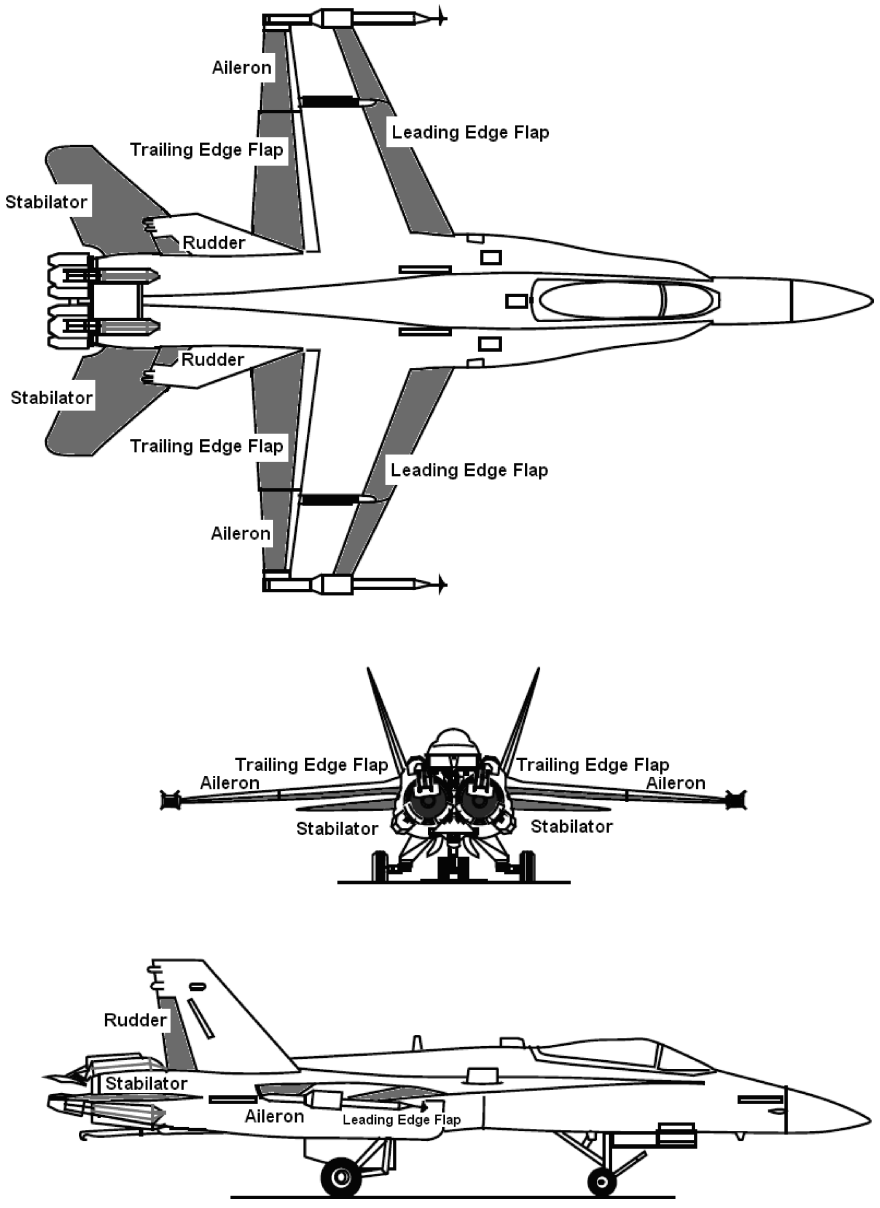


**Fig. 1 F-18 aircraft.**

states must be asymptotically stable. These requirements are similar to those employed in feedback linearization designs.

3) The sliding manifolds for each control channel are selected. For the current application, each of the channels of step 2 has a relative order of 1.

a) This means that the manifolds $\sigma$ for each channel can be given by

$$\sigma = K_0 e(t) + K_1 \int e(t)\,\mathrm{d}t \tag{2}$$

where $e(t)$ refers to the error signal in either channel [e.g., $p_c(t) - p(t)$, with $p_c(t)$ representing a roll-rate command, assumed here to be created by pilot inputs].

b) Because a boundary layer will be used to eliminate high-frequency switching of the control signal [12], the control law implemented by Eq. (2) is expressed in transfer-function form as

$$u(s) = \frac{\rho}{\varepsilon}\sigma = K_\rho\left(K_0 + \frac{K_1}{s}\right)\sigma \tag{3}$$

where $u(s)$ is the output of the SMC system for either loop and $\varepsilon$ is the boundary-layer thickness. The parameters $K_\rho$, $K_1$, and $K_0$ are chosen to provide desirable properties in the frequency domain: that is, loop transmissions with broad $K/s$-like characteristics around the crossover frequency [14]. No actuator dynamics are included in this step. The design can be conducted in a sequential loop-by loop fashion.

4) With the $K$ values just determined, the existence of sliding modes are verified through computer simulation. As in step 3, no actuator dynamics are included.

5) A boundary layer is included in the controller to eliminate the high-frequency switching in the control signals $u(t)$ from step 4. Again, no actuator dynamics are included.

6) Actuator dynamics are included in the computer simulation. Instability will almost certainly result.

7) Asymptotic observers are created for each channel. Actuator dynamics are eliminated in the vehicle model used in the observer. The eigenvalues of the observers are selected as real and (approximately) equal. The eigenvalues are determined in the frequency domain based upon the stability margins and shape of effective unity-feedback-loop transmissions.

8) To increase robustness, hedge dynamics are created. Additional rate feedback may be included in the control loops to add robustness to unmodeled time delays.

9) If desired, the observers of step 7 can be scheduled with the flight condition.

**Table 1 Flight conditions examined in [13]**

| Flight condition | Velocity, Mach | Altitude, ft | Angle of attack, deg | Dynamic pressure, lbf/ft$^2$ |
|---|---|---|---|---|
| 1 | 0.22 | 5000 | 22.9 | 59.7 |
| 2 | 0.25 | 15,000 | 23.6 | 52.0 |
| 3 | 0.35 | 30,000 | 25.8 | 54.0 |
| 4 | 0.45 | 40,000 | 24.3 | 55.8 |
| 5 | 0.65 | 40,000 | 16.0 | 116.5 |
| 6[a] | 0.9 | 40,000 | 3.50 | 223.0 |
| 7[a] | 0.9 | 30,000 | 2.36 | 357.3 |
| 8[a] | 0.9 | 15,000 | 1.50 | 678.2 |
| 9[a] | 0.9 | 10,000 | 1.36 | 825.5 |
| 10[a] | 0.9 | 5000 | 1.21 | 999.4 |
| 11[a] | 0.6 | 5000 | 2.53 | 444.2 |
| 12 | 0.4 | 5000 | 2.24 | 197.4 |
| 13 | 0.25 | 10,000 | 18.1 | 63.7 |
| 14[a] | 0.9 | 9000 | 1.34 | 858.5 |
| 15 | 0.3 | 20,000 | 19.6 | 61.3 |
| 16 | 0.31 | 25,000 | 22.79 | 53.0 |
| 17 | 0.4 | 35,000 | 23.5 | 56.0 |
| 18[a] | 0.9 | 35,000 | 3.68 | 283.4 |
| 19[a] | 0.9 | 25,000 | 2.01 | 446.3 |
| 20[a] | 0.9 | 20,000 | 1.75 | 552.1 |
| 21[a] | 0.9 | 8000 | 1.30 | 892.2 |
| 22[a] | 0.9 | 7000 | 1.29 | 926.4 |
| 23[a] | 0.9 | 6000 | 1.27 | 962.2 |
| 24 | 0.7 | 40,000 | 9.00 | 135.1 |
| 25 | 0.7 | 35,000 | 5.22 | 171.4 |
| 26[a] | 0.7 | 30,000 | 4.26 | 216.1 |
| 27[a] | 0.7 | 25,000 | 3.51 | 270.0 |
| 28[a] | 0.7 | 20,000 | 2.93 | 334.0 |
| 29[a] | 0.7 | 15,000 | 2.49 | 410.2 |
| 30[a] | 0.7 | 10,000 | 2.12 | 499.4 |
| 31[a] | 0.7 | 5000 | 1.84 | 604.6 |

[a]Flight conditions chosen for study.

The description of the nine design steps was deliberately brief. Again, [3–11] provide more detailed information about the implementation of these steps. Reference [9] may be particularly helpful, as it represents the most recent application of the design technique.

## IV. Design Specifics

Figure 2 shows the control structure relative to steps 1 and 2. The control distribution matrix **W** in Fig. 2 was chosen to be identical to that used in [13] to allow a meaningful comparison of the two design approaches in what follows. The selection of this matrix forces attention to be focused upon the high-dynamic-pressure (low angle of attack) flight conditions of Table 1. For the lower-dynamic-pressure cases, exclusive use of the rudder for sideslip control is unadvisable due to the significant decrease in effectiveness of the rudder surfaces in these conditions. For example, the stability derivative $N_\delta$ for the rudder at flight condition 13 is only 12% of its value at flight condition 11. This would warrant a change in **W** for these flight conditions, an addition that was beyond the scope of this study. The necessity of altering the **W** for the low-dynamic-pressure cases was also noted in [13]. The matrix **W** is given by

$$\mathbf{W} = \begin{bmatrix} 1.0 & 0 \\ 0.333 & 0 \\ 0.0875 & 1.0 \\ 0.7333 & 0 \\ 1.0 & 0 \end{bmatrix} \tag{4}$$

To place transmission zeros in the left-half plane for the 19 flight conditions to be simulated, regulated variables were employed here [15]. This led to the definition of two regulated variables as

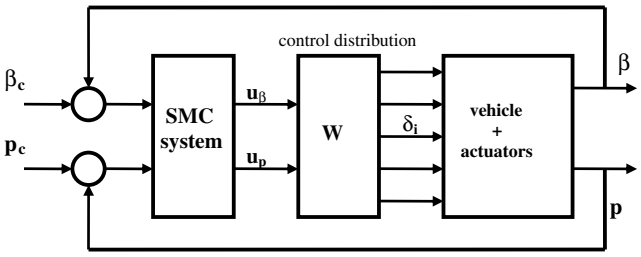


**Fig. 2 Basic control structure.**

$$\begin{aligned} p_{\text{reg}} &= p + K_1\beta \qquad K_1 = 0.3/\text{s} \\ \beta_{\text{reg}} &= \beta + K_2 r \qquad K_2 = -0.3\ \text{s} \end{aligned} \tag{5}$$

5) Fig. 3 shows the open-loop transfer functions $(p_{\text{reg}}/u_p)(s)$ and $(\beta_{\text{reg}}/u_\beta)(s)$. The controllers corresponding to Eq. (3) in step 3 were created as

$$u_p(s) = 75\left[0.1 + \frac{1}{s}\right]e_p(s) \qquad u_\beta(s) = 60\left[5.0 + \frac{1}{s}\right]e_\beta(s) \tag{6}$$

Figure 4 shows the resulting loop transmissions with the compensation of Eqs. (6). Note the very large crossover frequencies in evidence. This is a typical result at this juncture of the design [3–11]. Infinite-frequency control switching was in evidence with these controllers. Boundary layers were introduced to eliminate this

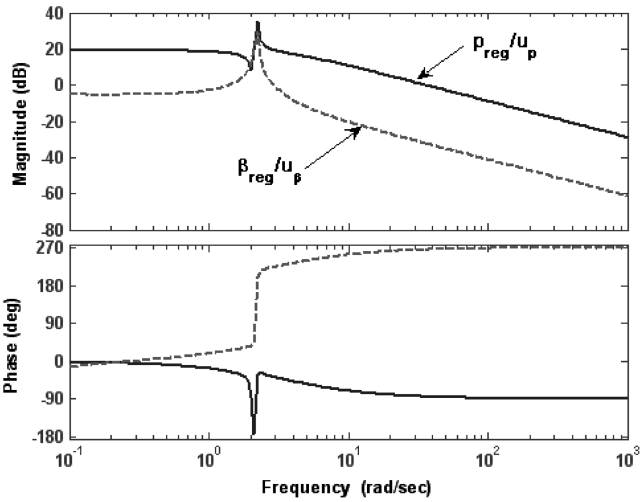


**Fig. 3 Bode diagrams of open-loop transfer functions (no actuators).**

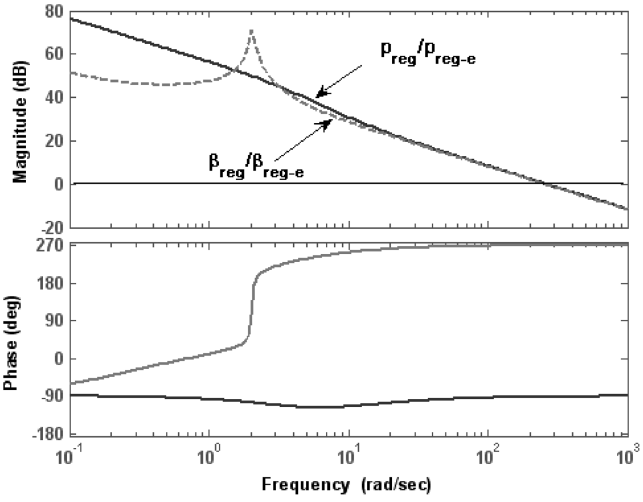


**Fig. 4 Bode diagrams of loop transmissions (no actuators).**

switching. However, as expected, the system was unstable when actuator dynamics were included.

An observer was designed for each of the two feedback loops. The observer eigenvalues were selected as follows:

For the $p$ loop:

$$\lambda_i = -2.2,\ -2.4,\ -2.6,\ -2.8 \text{ rad/s} \tag{7a}$$

For the $\beta$ loop:

$$\lambda_i = -1.65,\ -1.8,\ -1.95,\ -2.1 \text{ rad/s} \tag{7b}$$

Choice of the observer eigenvalues is based upon effective or equivalent unity-feedback-loop transmissions defined as

$$L_{\text{eq}-p} = \frac{p_{\text{reg}}/p_c}{1-(p_{\text{reg}}/p_c)} \qquad L_{\text{eq}-\beta} = \frac{\beta_{\text{reg}}/\beta_c}{1-(\beta_{\text{reg}}/\beta_c)} \tag{8}$$

These loop transmissions are those that would be exhibited by a system with unity feedback (no dynamics in the feedback loop and serial compensation) but with closed-loop dynamics identical to that of the SMC design. Actuator dynamics *are* included at this juncture. The desire to create a large frequency range in which the $k/s$-like dynamics are in evidence drives the selection of the observer eigenvalues. Figure 5 demonstrates the effects of observer eigenvalue selection on $L_{\text{eq}-p}$ for three cases: 0.2, 1.0, and 5 times the eigenvalues shown in Eq. (7) (identified as nominal). Note that the nominal eigenvalue selection of Eq. (7) offers a tradeoff between low-frequency magnitude and phase margin. The system with 5 times the nominal eigenvalues is seen to be unstable (negative phase margin).

The hedge dynamics were designed next. For each response variable, an additional loop is closed in parallel with the observer. This is shown in Fig. 6 for the $p$ loop. A similar structure exists for the $\beta$ loop. Note that no measurement of actuator output is required in this formulation.

The purpose of the hedge dynamics is to further decrease the destabilizing effects of the actuator dynamics. The compensation in these loops is created from Bode plots as follows (e.g., [10]). The magnitude plot of the hedge dynamics should exhibit a 1) $+20$ dB/decade slope at low frequencies, 2) $-20r$ dB/decade slope at frequencies around the frequency of the actuator bandwidths [here, $r$ is the relative order of the vehicle dynamics in the loop in question (without actuators)], and 3) $-20r$–20 dB/decade slope at high frequencies.

The gain on the resulting transfer functions are adjusted so that the maximum magnitude of the Bode diagram of the hedge dynamics equals that of the Bode diagram of $(\hat{y}_i/u_{y_i})(s)$ in the frequency region near the average actuator bandwidths servicing the loop in question. Here, $\hat{y}_i$ is the estimate of the response variable $y_i$ (output of the observer), and $u_{y_i}$ is the output of the SMC block controlling $y_i$. Figure 7 shows the results of this procedure for the roll-rate loop.

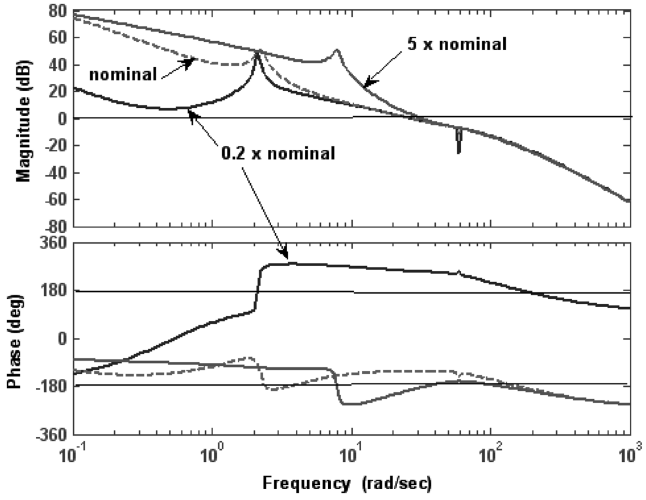


**Fig. 5 $L_{\text{eq}-p}$ for eigenvalues of 0.2, 1.0 and 5 times the nominal values of Eq. (7).**

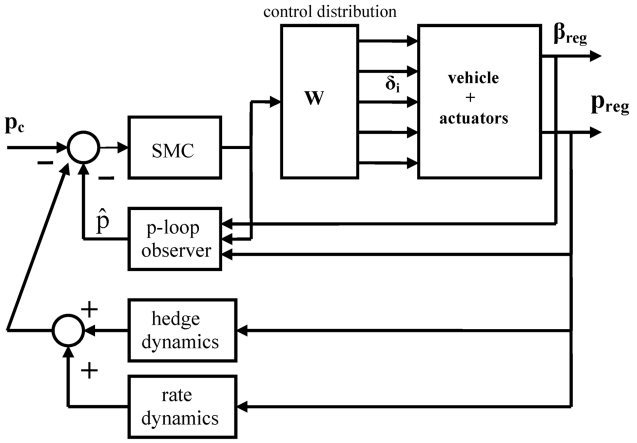


**Fig. 6 Hedge and rate dynamics in the SMC design.**

The penultimate design step involves the addition of an additional rate loop in parallel with both the observer and hedge dynamics. This loop was found to be beneficial in [9] to increase system robustness in the presence of unmodeled time delays. This added compensation essentially modifies the hedge dynamics. The final hedge and additional rate dynamics are given as follows:

Hedge dynamics for the $p$ loop:

$$\frac{6000s}{s^3+208s^2+1616s+3200} \tag{9a}$$

Hedge dynamics for the $\beta$ loop:

$$\frac{178s}{s^3+220s^2+4100s+20,000} \tag{9b}$$

Rate dynamics for the $p$ loop:

$$\frac{0.005s}{0.0002s+1} \tag{10a}$$

Rate dynamics for the $\beta$ loop:

$$\frac{0.01s}{0.002s+1} \tag{10b}$$

Figure 8 shows the Bode diagrams of the transfer functions defined in Eq. (8), now including the hedge dynamics and additional rate

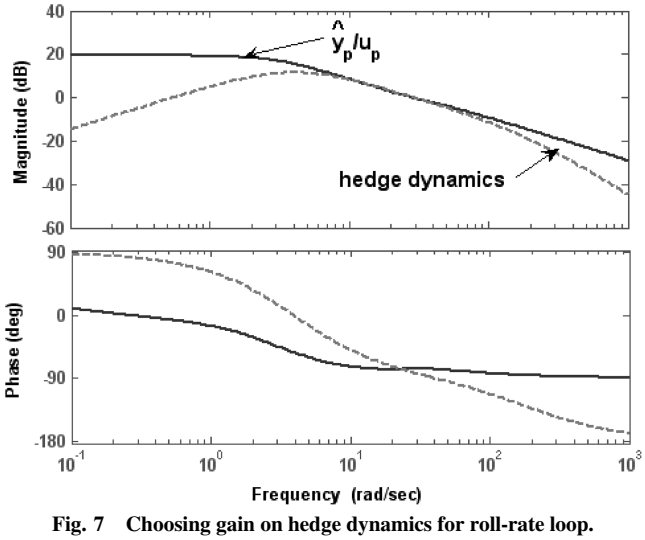


**Fig. 7 Choosing gain on hedge dynamics for roll-rate loop.**

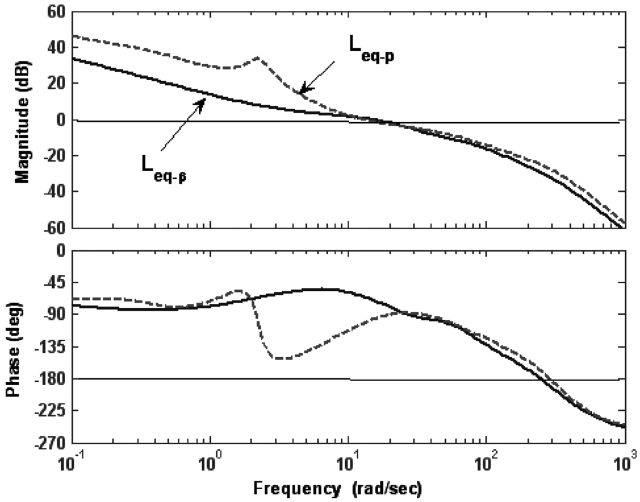


**Fig. 8 Bode plots of effective unity-feedback-loop transmissions (actuators, observers, hedge, and rate dynamics included).**

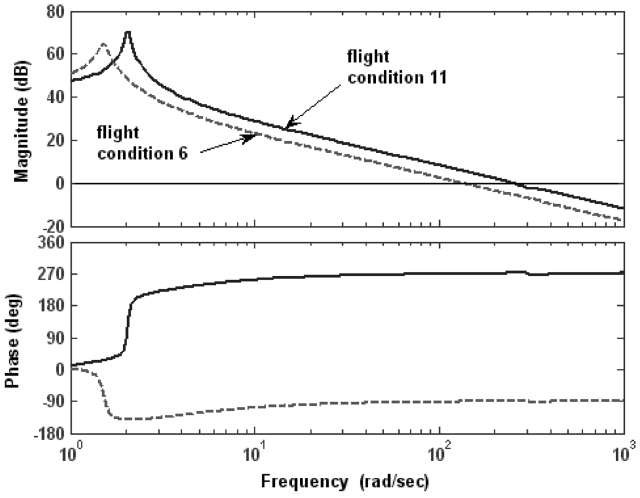


**Fig. 10 Bode diagrams for loop transmissions $[\beta_{\text{reg}}/(\beta_{\text{reg}} - e)](s)$ corresponding to Fig. 4 for flight conditions 6 and 11.**

feedback. Average phase and gain margins of 96 deg and 28 dB are in evidence, respectively, with $K/s$-like dynamics in evidence around crossover. Also note the significant decrease in crossover frequencies from those exhibited in Fig. 4.

Figure 9 shows the final system closed-loop transfer functions. Note that the $p$ and $\beta$ that are indicated are not the regulated variables, but the variables that would be observed by the pilot. Finally, a command filter was added on the pilot-input roll-command inputs to reduce the roll-rate bandwidth. The original high-bandwidth roll-rate-command system may have produced a design susceptible to oscillatory pilot/vehicle behavior such as roll ratchet [16]. This filter was described by

$$G_{\text{filter}} = \frac{10^2}{s^2 + 20s + 10^2} \tag{11}$$

Finally, the observers (and *only* the observers) were scheduled with flight condition. The desired eigenvalues remained unchanged, but the observer gains necessary to obtain these eigenvalues were scheduled. This simplified scheduling technique is possible because the forms of the open-loop transfer functions for the vehicle model (shown in Fig. 4) are relatively invariant with flight condition. This characteristic is demonstrated in Fig. 10, in which the Bode plots for $[\beta_{\text{reg}}/(\beta_{\text{reg}} - e)](s)$ are shown for flight conditions 6 and 11. These plots correspond to the Bode plot of $[\beta_{\text{reg}}/(\beta_{\text{reg}} - e)](s)$ in Fig. 4. This SMC characteristic was first exploited in [8] for an entirely different class of vehicle. It is not claimed that the high-frequency characteristics of Fig. 10 are an accurate representation of those of the actual aircraft. For example, any number of structural modes will be in evidence in this frequency range. For the vehicle models given, however, creating sliding manifolds such as those of Eqs. (6) would result in compensation elements that differ only slightly. The deviations from the characteristics of the actual vehicle will constitute parasitic dynamics for which the effects on closed-loop performance are minimized by the observer(s) [3–11].

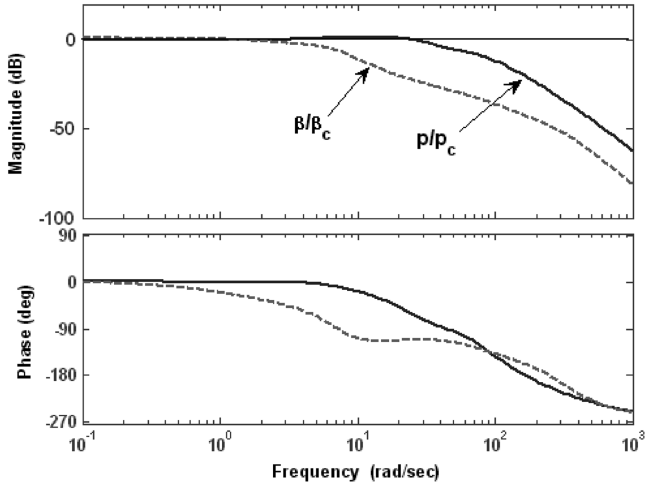


**Fig. 9 Bode plots of closed-loop transfer functions.**

## V. Pilot Model

The task at hand will involve only roll-attitude tracking; that is, the pilot is assumed to be flying with feet on the floor with no pedal inputs. The pilot model to be used is the structural model of the human pilot [17]. The model is shown in Fig. 11. In the current application, the vestibular feedback path will not be used.

In addition to the model itself, predictions of handling-quality levels are possible [17]. These predictions involve the use of a handing-quality sensitivity function (HQSF). The HQSF is defined as

$$\text{HQSF} = \frac{1}{K_e}\left|\frac{U_M}{C}(j\omega)\right| \tag{12}$$

where $K_e$ is the gain appearing in $Y_e$. In this application $Y_e = K_e$. As will be seen, handling-quality levels are predicted based upon whether the HQSF violates well-defined bounds in a plot of HQSF vs frequency. For this evaluation, the crossover frequency of the pilot/vehicle system is set to 2.0 rad/s [17].

The elements of the pilot model for the design flight condition (flight condition 1) are given as follows:

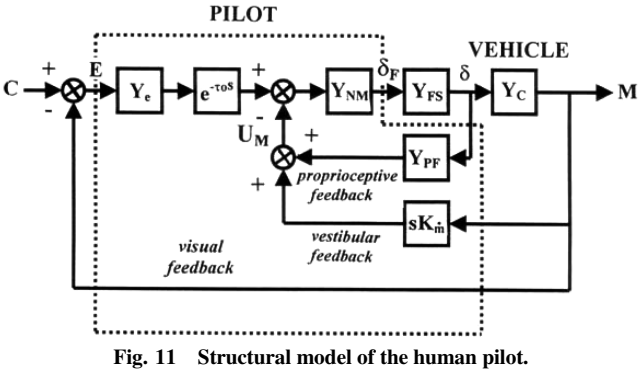


**Fig. 11 Structural model of the human pilot.**

Feel system (FS):

$$Y_{\mathrm{FS}} = \frac{25^2}{s^2 + 2(0.6)25s + 25^2} \tag{13}$$

Neuromuscular (NM) dynamics:

$$Y_{\mathrm{NM}} = \frac{10^2}{s^2 + 2(0.7)10s + 10^2} \tag{14}$$

Time delay:

$$\tau_0 = 0.2 \text{ s} \tag{15}$$

Outer-loop equalization (for 1.5 rad/s crossover frequency):

$$Y_e = 4.15 \tag{16a}$$

Outer-loop equalization (for 2.0 rad/s crossover frequency):

$$Y_e = 5.70 \tag{16b}$$

Proprioceptive dynamics:

$$Y_{\mathrm{PF}} = 1.54 \tag{17}$$

The normalization procedure that is used in closing the innermost loops (proprioceptive feedback) in the pilot model of Fig. 11 eliminates the need for units to be attached to the elements of Eqs. (13–17). Figure 12 shows the Bode plot of the open-loop pilot/vehicle transfer function for the design flight condition, demonstrating that the dictates of the crossover model of the human pilot were followed in the structural model formulation [18]. A 1.5 rad/s crossover frequency is employed for tracking (as opposed to handling-quality prediction) and is representative of values obtained from in-flight measurements in roll-tracking tasks of fighter aircraft (e.g., [19]). Two unmodeled time delays of 0.20 s (computational and sensor-related) were included in creating the Bode diagram of Fig. 12.

## VI. Postdamage Pilot-Induced Oscillations

Damage-tolerant flight control system designs should include some measures to reduce the possibility of pilot-induced oscillations (PIOs) *after* damage has occurred. Even with control architectures that attempt to minimize the effects of damage on the control/response characteristics of the vehicle, sudden changes in the handling qualities of the vehicle after damage may be inevitable. The simplest technique to reduce the likelihood of PIOs is to reduce the command gain in the pilot's control channel after damage. With the proposed design procedure, the simplest way to determine that

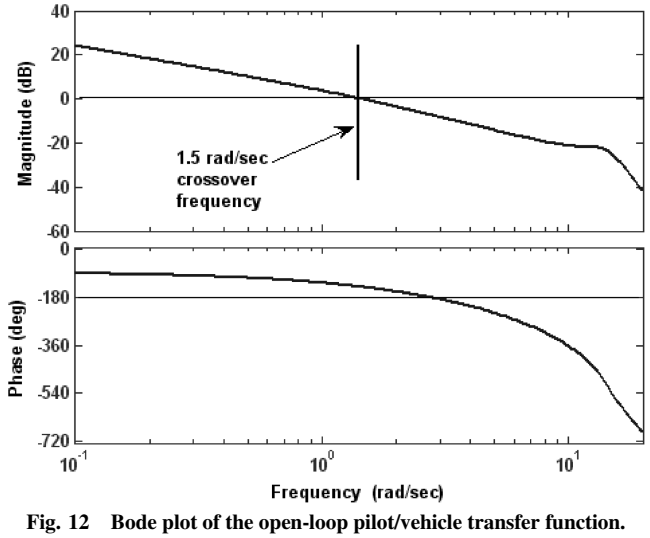


**Fig. 12 Bode plot of the open-loop pilot/vehicle transfer function.**

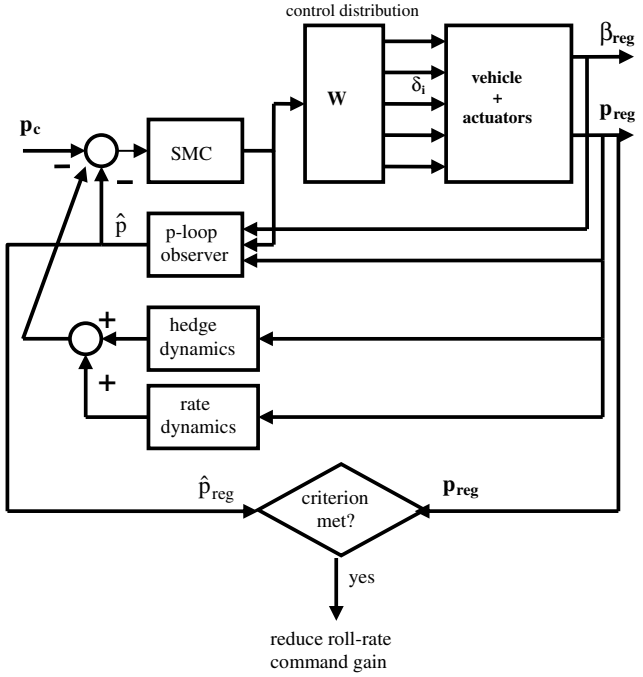


**Fig. 13 Modified control architecture to minimize PIO.**

damage or failure has occurred is to compare the estimate(s) of the vehicle response variable provided by the observer with measured values (i.e., use the observer residuals). This technique has been proposed in Kalman filtering applications (e.g., [20]). Here, this means comparing $\hat{p}_{\mathrm{reg}}$ with the measured roll rate $p_{\mathrm{reg}}$. If this difference exceeds some criterion value, the command-gain in the roll-rate channel can be reduced. This modified control architecture in shown in Fig. 13. Based upon preliminary computer simulation, a criterion value defined as $|\hat{p}_{\mathrm{reg}} - p_{\mathrm{reg}}| > 20$ deg/s was selected. This criterion value is of obvious importance. Too small of a value can cause the criterion to be exceeded by a healthy aircraft encountering turbulence. Too large of a value may increase the likelihood of pilot-induced oscillations after damage. The choice of a criterion value of 20 deg/s was primarily based upon expediency here. The pilot command gain was reduced by 50% in the computer simulations to be described. Of the two values just described (i.e., the response rate criterion and the percentage of command-gain reduction), the former is undoubtedly the more critical. A number of issues arise here, not the least of which is the quality of the vehicle model used in the estimator design and implementation. Appealing to formal failure-detection algorithms might well defeat the purpose of the SMC approach: namely, instantaneous accommodation to vehicle damage. As a start, one might consider the effect of false positives in the damage-detection criterion and identify handling-quality issues that would arise in such cases through piloted simulation.

## VII. Pilot/Vehicle Performance

### A. Handling Qualities

Figure 14 shows the HQSF for roll control for the undamaged aircraft at flight condition 11. Only level 2 handling qualities are predicted. No requirement for handling qualities was made after failure, as only stability and acceptable performance are desired. The disappointing handling-quality prediction was improved by simply modifying the command-path filter of Eq. (11) to that given next, in which additional lead was provided beyond 5 rad/s. Figure 15 shows the modified HQSF, now predicting level 1 handling qualities.

$$G_{\mathrm{filter}} = \frac{10^2(0.2s + 1)}{s^2 + 10s + 10^2} \tag{18}$$

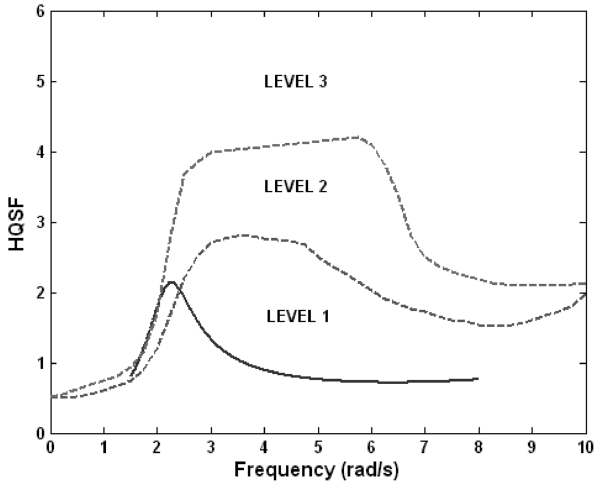


**Fig. 14 HQSF for roll control with no damage for flight condition 11.**

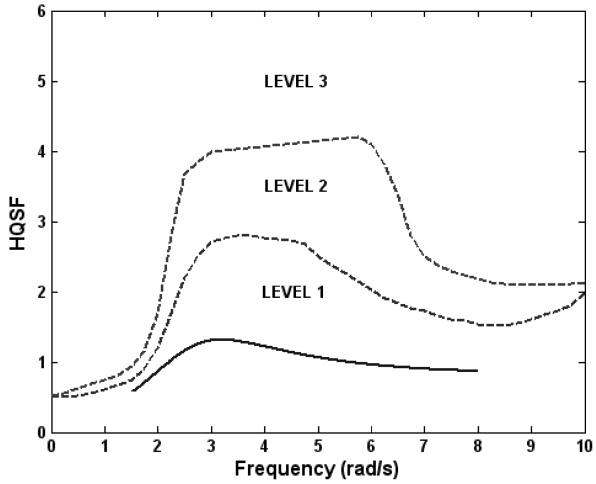


**Fig. 15 HQSF for roll control with no damage for flight condition 11 and a modified command-path filter.**

### B. Nominal System Simulation

Pilot/vehicle tracking performance at the design flight condition (flight condition 11) was examined through computer simulation. Unmodeled vehicle characteristics were included in the nominal undamaged vehicle. These characteristics included the time delays mentioned earlier:

1) A 0.02 s time delay models computational and possible actuator delays.

2) A 0.02 s time delay models sensor delays.

3) Sensor noise with rms values of 0.35 deg/s ($p_{\text{reg}}$) and 0.35 deg ($\beta_{\text{reg}}$) is created by passing white noise through second-order filters with unity damping ratio and break frequencies of 10 rad/sec

4) A dipole emulates the effects of an unmodeled flexible mode. The dipole was added to all the vehicle response variables and was of the form

$$G_{\text{structrual}} = \frac{60[s^2 + 2(0.01)50s + 50^2]}{50[s^2 + 2(0.01)60s + 60^2]} \tag{19}$$

Figure 16 shows the effect of the dipole dynamics on the closed-loop transfer function $(\phi/p_c)(s)$.

5) There are amplitude and rate limits on all actuators (see Appendix A for these limits).

6) A sensor noise filter on the sideslip signal has the form given by

$$\beta_{\text{filter}} = \frac{25^2}{s^2 + 2(1.0)25s + 25^2} \tag{20}$$

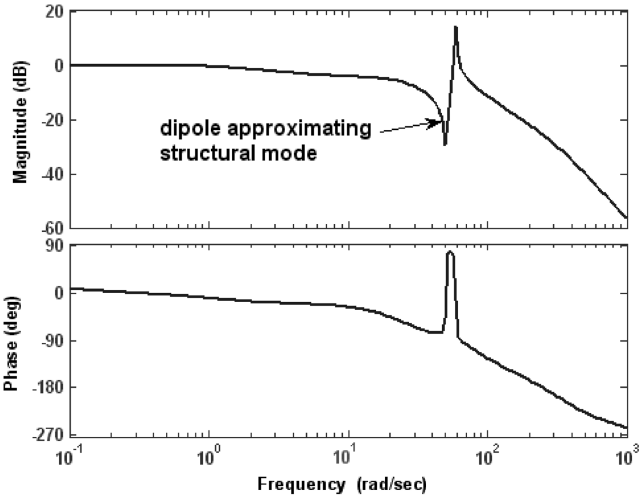


**Fig. 16 Bode plot of $(\phi/p_c)(s)$ transfer function showing the effect of the unmodeled dipole.**

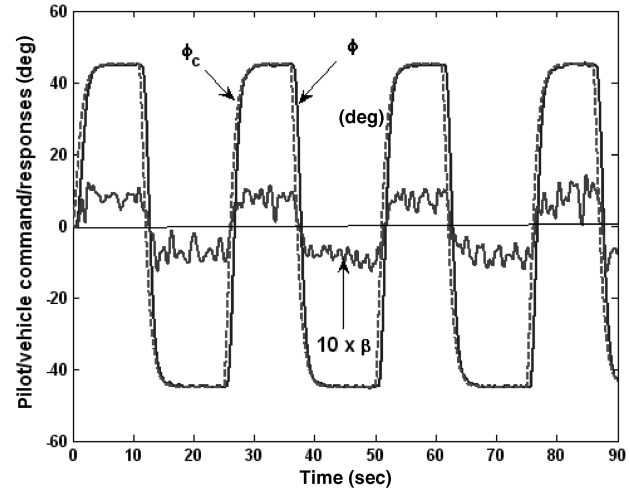


**Fig. 17 Pilot/vehicle performance with no damage for flight condition 11.**

Figure 17 shows the pilot/vehicle response to a series of filtered-step roll-attitude commands of ±45 deg. Performance is seen to be excellent. Figures 18 and 19 show the resulting control-surface deflections (note the different time scales in Figs. 18 and 19

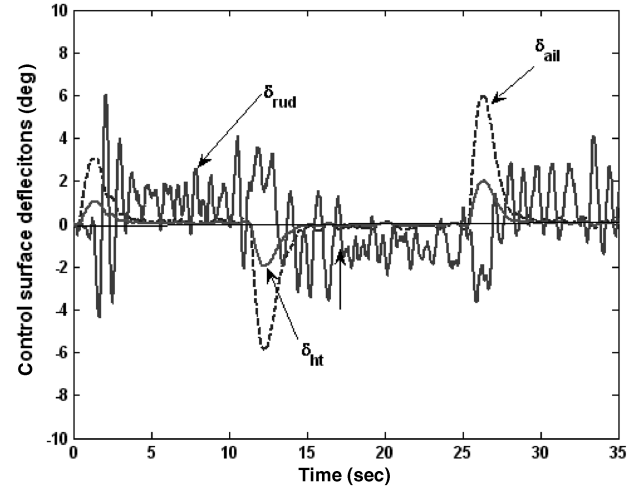


**Fig. 18 Aileron, rudder, and horizontal tail displacements with no damage.**

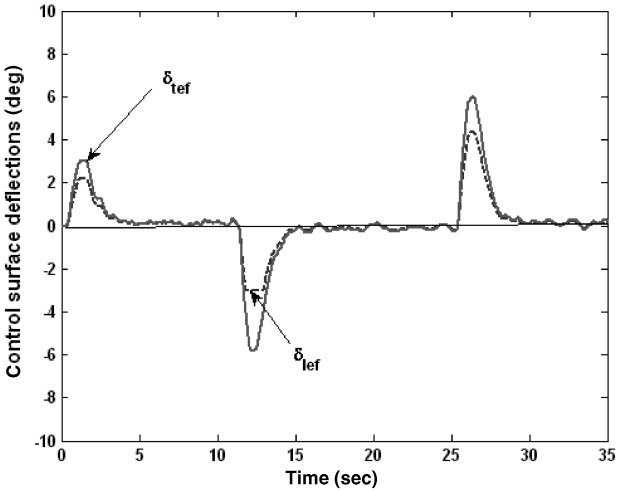


**Fig. 19 Leading- and trailing-edge flap displacements with no damage.**

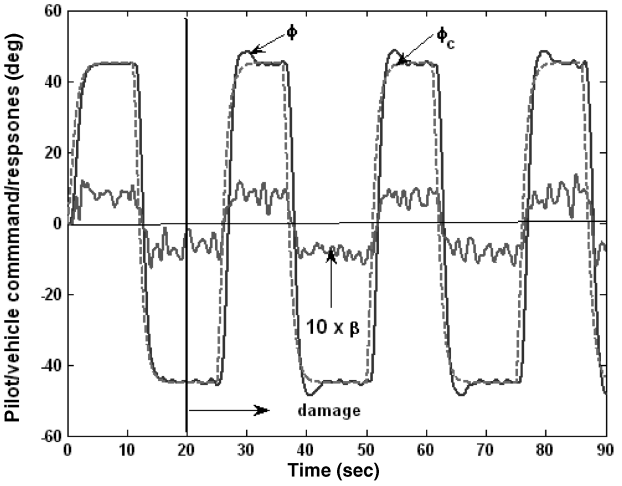


**Fig. 21 Pilot/vehicle performance with damage at $t = 20$ s for flight condition 11.**

compared with Fig. 17). The rudder activity evident in Fig. 18 is directly attributable to sensor noise. This rudder activity is not surprising, as the injected noise had frequent maximum values of $\pm 1$ deg in the $\beta_{\text{reg}}$ loop, which was of the same order of magnitude as $\beta_{\text{reg}}$ itself.

### C. Damaged System Simulation

Using the same task as in the simulation of Sec. VII.B, a computer simulation was conducted with a damaged system. The damage consists of the following: a 50% reduction in the effectiveness of all the control effectors, modeled as a reduction in the command gain to the actuators; an additional 0.05 s time delay placed immediately before the actuators; and the addition of a 5 deg backlash element in all the actuator models. This element is shown in Fig. 20 for the aileron actuator. This model is based upon an example of a worn or damaged actuator taken from [21].

The term *damage* must be interpreted somewhat loosely here. The damage consists of easily implemented system changes that are inimical to closed-loop stability and performance. The damage or failures occur 20 s into the tracking run. Figure 21 shows the pilot/vehicle responses, and Figs. 22 and 23 show the control-surface deflections. Although obviously degraded from the no-damage condition, pilot/vehicle performance is still acceptable. It is interesting to note that the 50% reduction in control effectiveness does not result in a concomitant reduction in control displacements after damage occurs. This is a result of the SMC design and contributes to the robustness of the system. The pilot command gain was not reduced in this configuration after damage. The pilot model described in Fig. 11 and Eqs. (13–17) was not changed for any of the damaged simulations. It was felt that this provided a challenging restriction for the design; that is, no changes in pilot dynamic compensation were permitted to accommodate any changes in the overall command/response characteristics of the aircraft.

### D. Performance Comparison

The claimed robust properties of the SMC design should be supported by a comparison with a competing design approach. To

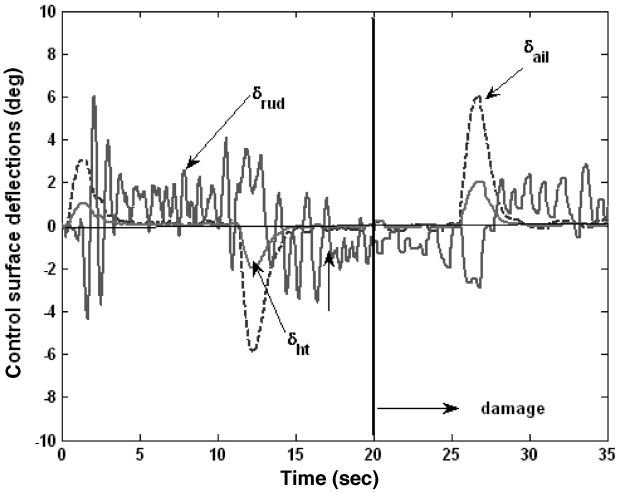


**Fig. 22 Aileron, rudder, and horizontal tail deflections with damage at $t = 20$ s.**

this end, the quantitative feedback theory (QFT) design described in [13] applied to the same vehicle model was simulated. Table A1 lists the actuator position and rate limits. The QFT design is given in Appendix A. Fairness would dictate our emphasizing that the design of [13] was not claimed to be robust against the types of simulated damage used here. Rather, [13] provides a detailed treatment of a QFT design that was created to handle the same set of flight conditions as that used here, without the need for scheduling. The QFT approach is, however, well known for its robust properties (e.g., [22]). To simplify the comparison, flight condition 11 was used, and none of the unmodeled characteristics for the undamaged vehicle described in Sec. VII.A were included. In addition, no pilot model was used. Instead, a roll-rate command similar to that in evidence with the SMC design was used as a command to the QFT system. The only damage that was considered was the 5 deg actuator backlash

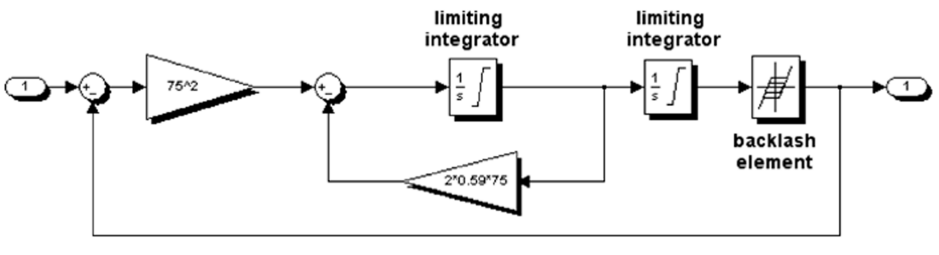


**Fig. 20 Actuator model with a backlash element.**

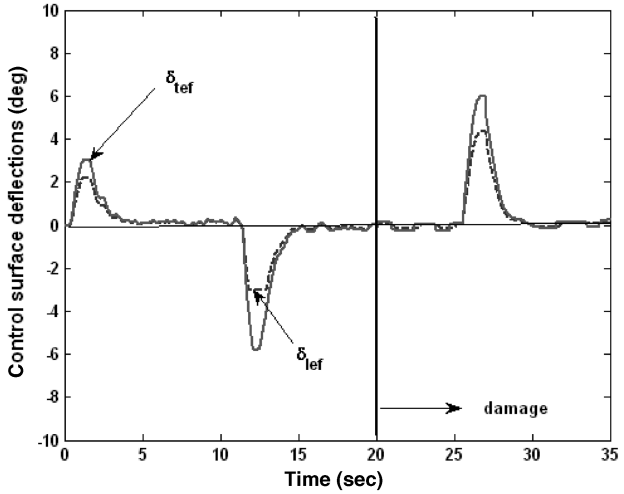


**Fig. 23 Leading- and trailing-edge flap deflections with damage at $t = 20$ s.**

(and then only in the aileron and rudder actuators). Figure 24 shows the results. The system is seen to exhibit instability shortly after the damage was introduced at $t = 20$ s.

### E. Performance for 19 Flight Conditions

Figure 25 is a composite of the pilot/vehicle responses for the SMC design for each of the 19 flight conditions called out by the footnote in Table 1. As can be seen, after damage, stability is evident throughout, although it rarely matches the performance of the nominal (undamaged) vehicle. Note the quality of the responses for all 19 flight conditions before damage occurs. Finally, 6 of the 19 runs resulted in the pilot command gain being reduced after damage. The conditions that did result in reduced command gain were flight conditions 9, 10, 14, and 21–23. The roll-attitude responses exhibiting large overshoot are the six conditions for which the pilot command gain was reduced after damage. Further examination of these conditions indicated that if the pilot were to compensate for the command-gain reduction sometime after damage, the roll-attitude tracking performance would be restored. This does not necessarily imply that the original command-gain reduction was unnecessary, as sudden changes in vehicle dynamics have been identified as triggering events for PIOs [23].

The quality of the tracking performance across the 19 flight conditions without damage when the pilot model was unchanged strongly suggests that level 1 handling qualities would be predicted for each of the flight conditions. To support this contention, the HQSF was calculated for flight conditions 6, 10, and 11. These were

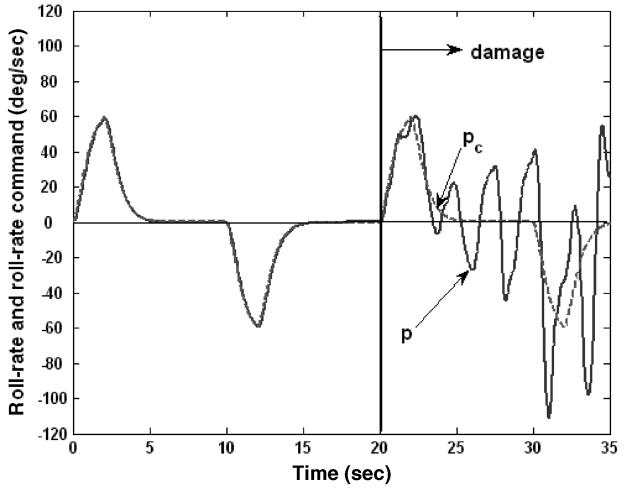


**Fig. 24 Roll-rate tracking performance for the QFT design of [13].**

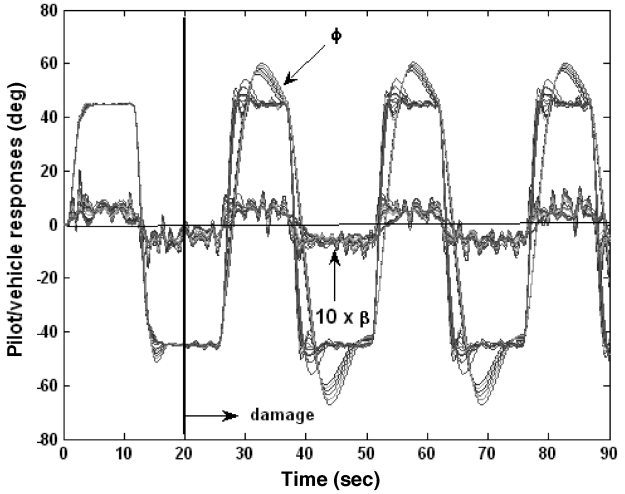


**Fig. 25 Composite of pilot/vehicle performance for 19 flight conditions.**

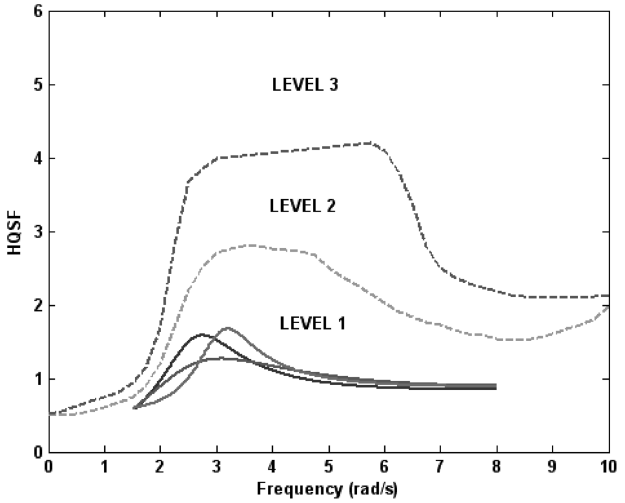


**Fig. 26 HQSF for roll control with no damage for flight conditions 6, 10, and 11 and a modified command-path filter.**

chosen because of the disparate dynamic pressures, altitudes, and Mach numbers in evidence for these conditions (see Table 1). Figure 26 shows the HQSF results, clearly indicating level 1 handling qualities.

## VIII. Critique and Discussion

Formal stability proofs were conspicuously absent from the research summarized herein. As pointed out in [11], in SMC designs, this question is typically addressed through Lyapunov stability criteria with the goal of guaranteeing global attractiveness of the sliding manifold (i.e., the so-called *reaching condition* [24]). The interpretation of pseudo-sliding-mode design in the frequency domain merely means that *linear* stability can be ascertained through application of linear techniques such as the Nyquist criterion, with its associated gain and phase margin measures. This was alluded to in the discussion of Fig. 8. Analytically guaranteeing stability when the vehicle undergoes significant changes in dynamics can be quite difficult. This is attributable to the fact that damage scenarios can result in actuator saturation, thus precluding linear stability analyses. This possibility is demonstrated in Figs. 27 and 28. For the sake of exposition, the rate limits on the rudder actuator were reduced from $\pm 82$ to $\pm 10$ deg/s for flight condition 11. This is in addition to the damage described in Sec. VII.C. Figure 27 shows the resulting tracking performance, and Fig. 28 shows the rudder deflection rate. Because of the possibility of highly nonlinear actuator output, the authors have simply opted for computer simulation to demonstrate

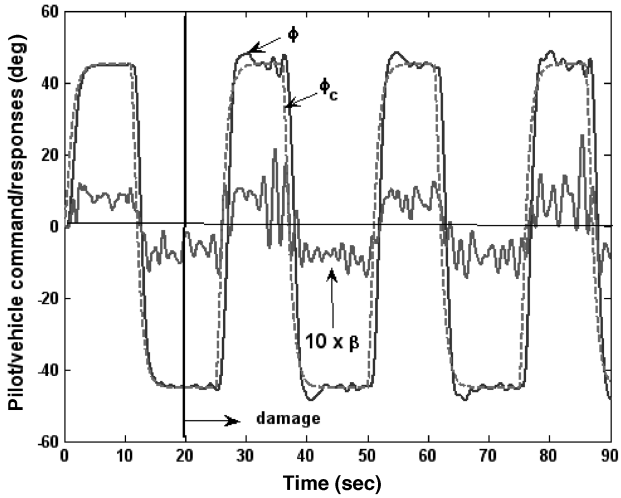


**Fig. 27 Pilot/vehicle performance with damage at $t = 20$ s, including reduced rudder rate limits and flight condition 11.**

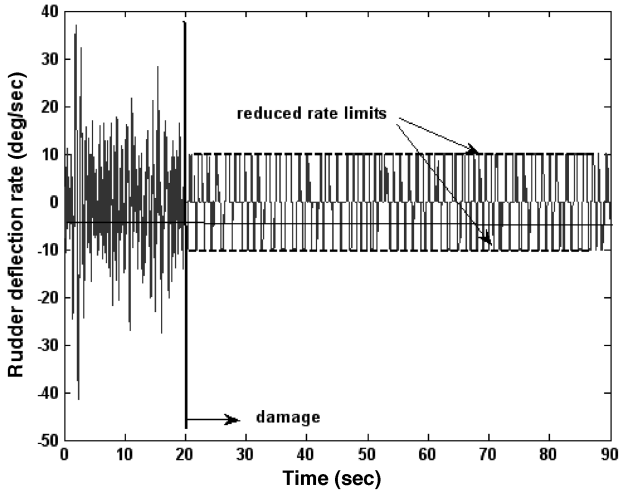


**Fig. 28 Rudder deflection rate for performance of Fig. 27.**

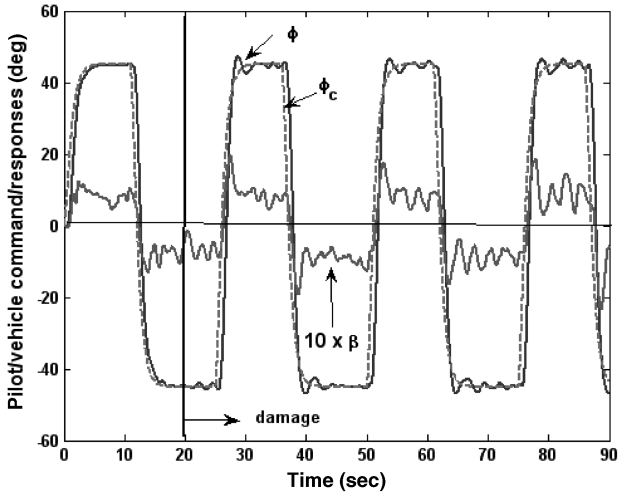


**Fig. 29 Pilot/vehicle performance with damage at $t = 20$ s, flight condition 11 digital control-law implementation, and 25 hz sampling frequency.**

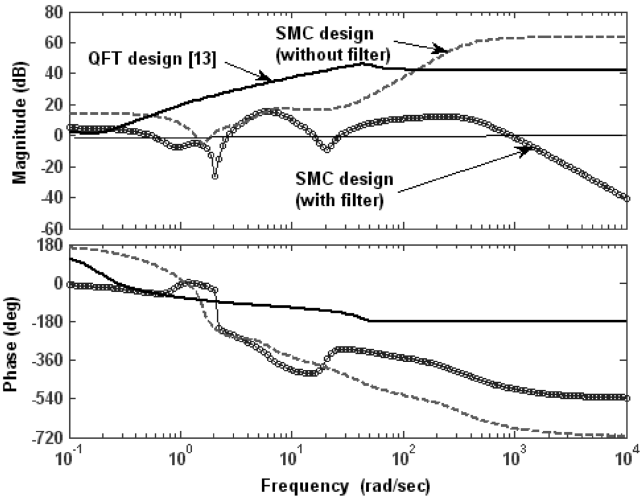


**Fig. 30 Bode plot of transfer functions between $\beta$-loop controller outputs and injected $\beta_{\text{reg}}$ and $\beta$ sensor noise for sliding-mode design and QFT design of [13].**

stability in the research reported herein. This is, of course, in addition to the linear measures provided by classical stability margins.

The synthesis technique is obviously not algorithmic in nature; that is, it requires a series of design decisions, most of which are based upon well-established frequency-domain measures. As in most aerospace designs, the creation of an acceptable control system will depend upon the experience of the practitioner. The authors do not view this fact as a handicap.

The control system design that resulted from this study is of relatively high order. The vehicle and actuator models, in total, describe a 14th-order system. The complete controller (including hedge dynamics, additional rate-feedback dynamics, and the command-path filter dynamics) was of the 20th order. By comparison, the QFT controller of [13] was only of the sixth order. A comparison with adaptive flight control architectures, however, suggests that the design developed here is relatively simple. Reference [25] provides one such adaptive design applied to a similar vehicle and flight control task.

The bandwidth of the $p/p_c$ loop evident in Fig. 9 would appear to require a high sampling rate in a digital implementation of the control law. For example, using the rule of thumb of sampling at least 20 times the bandwidth of the highest-bandwidth loop would appear to require an extraordinarily high sampling rate of 160 Hz) [26]. This design, however, has exhibited considerable robustness to computational delays, and the stability margins indicated in Fig. 8 may reduce the sampling requirement considerably. By way of demonstration, Fig. 29 shows the pilot/vehicle performance with the control law discretized with a Tustin transform at a relatively slow sampling rate of 25 Hz. By comparison, the fastest loop in the flight control computer of current operational F-18 aircraft is 80 Hz.[‡] The control law here includes Eqs. (6), the observers, hedge dynamics, and rate-feedback elements for both the roll-rate and sideslip loops, resulting in a single discrete state-space representation of the 18th order [the command filter of Eq. (18) was not discretized]. Flight condition 11 is chosen. All former system limitations are included, save for the 0.02 s computational/actuator delay. As might be expected with this low sampling rate, performance is degraded from that of Fig. 21, but still can be considered acceptable. Maximum sideslip excursions approaching 2.0 deg are now in evidence.

Designs resulting from the technique discussed here can be sensitive to sensor noise. This sensitivity manifests itself as increased control activity and has been pointed in other applications (e.g., [8]). This sensitivity is exemplified in Fig. 30, showing the Bode plots for the transfer functions between the output of the $\beta$-loop controllers (before **W**) and sensor noise injected in parallel with $\beta_{\text{reg}}$ (sliding-mode design) and $\beta$ (QFT design). This comparison was done without the unmodeled characteristics in the sliding-mode design that were enumerated in Sec. VII.B. Note the increased magnitude

[‡]Private communication with Shawn Donley, U.S. Naval Air Systems Command, Patuxent River, Maryland, 6 December 2007.

associated with the sliding-mode design at high frequency. This sensitivity was effectively minimized here by the addition of the sensor noise filter, as shown in the figure.

As was discussed in Sec. II, the vehicle model employed in this study is linear, and the lateral/directional dynamics were decoupled from the longitudinal. The authors are well aware of the model's simplicity. The selection of this model was predicated on its ready availability for a variety of flight conditions as well as the availability of an existing design for performance comparisons. The appropriate uniform resource locator for accessing [13] is included in the reference list. Thus, all the system descriptions are available to the reader who may be interested in verifying the results reported herein or in comparing performance with competing damage-tolerant or damage-adaptive system designs.

Finally, although described as an SMC design, the sliding-mode approach serves only as a convenient means to an end, that end being the creation of a robust control design through frequency-domain synthesis.

## IX. Conclusions

Based upon the research reported herein, the following conclusions can be drawn.

1) A pseudo-sliding-mode design technique interpreted in the frequency domain can provide an approach to damage-tolerant flight control system design. The step-by-step design procedure can be completed using simple Bode plots as the primary synthesis tool.

2) Over a broad set of flight conditions, scheduling of the sliding-mode design could be accomplished by scheduling only the asymptotic observers with the flight condition.

3) Level 1 handling qualities were predicted at the design flight condition and at two additional flight conditions with Mach numbers, altitudes, and dynamic pressures significantly different from those of the design condition.

4) By comparing the values of the estimated vehicle response variables with measured response variables, a simple technique could be established for reducing pilot command gains in an effort to reduce the likelihood of pilot-induced oscillations.

5) A brief comparison with a robust flight control design created for the same vehicle and flight conditions demonstrated the superiority of the sliding-mode design when damage was considered.

6) In comparison with competing designs, the pseudo-sliding-mode design technique discussed here may exhibit increased control activity that is attributable to sensitivity to sensor noise.

## Appendix A: Nominal Vehicle Characteristics for Flight Condition 11 Vehicle Description

For $\dot{\mathbf{x}} = \mathbf{A}\mathbf{x} + \mathbf{B}\mathbf{u}$,

$$\{x\} = \{p,\ r,\ \beta,\ \phi\}^T \qquad \{u\} = \{\delta_{\text{ail}},\ \delta_{\text{ht}},\ \delta_{\text{rud}},\ \delta_{\text{lef}},\ \delta_{\text{tef}}\}^T$$

For flight condition 11,

$$A = \begin{bmatrix} -3.54752 & 0.733331 & -14.5997 & -0.000019 \\ -0.014746 & -0.190622 & 4.532750 & 0.000490 \\ 0.043383 & -0.997810 & -0.280585 & 0.048805 \\ 1.0 & 0.043427 & 0 & 0 \end{bmatrix}$$

$$B = \begin{bmatrix} 14.794500 & 15.275300 & 4.41541 & 0 & 15.372300 \\ -0.210880 & 0.110922 & -2.709220 & -0.000004 & -0.173085 \\ -0.003891 & -0.010900 & 0.056915 & 0 & 0 \\ 0 & 0 & 0 & 0 & 0 \end{bmatrix}$$

**Table A1 Actuator amplitude and rate limits[a]**

| Surface | Position limits, deg | Rate limits, deg /s |
|---|---|---|
| Leading-edge flap | +33, −3 | ±15 |
| Trailing-edge flap | +45, −8 | ±18 |
| Aileron | +45, −25 | ±100 |
| Stabilator | +10.5, −24 | ±40 |
| Rudder | ±30 | ±82 |

[a]**A** and **B** matrices for the remaining flight conditions can be found in [13] in the reference list of the main body of the paper.

The actuator dynamics are as follows:

Aileron:

$$\frac{75^2}{s^2 + 2(0.59)75s + 75^2}$$

Differential horizontal tail:

$$\frac{35^2}{s^2 + 2(0.71)35s + 35^2}$$

Rudder:

$$\frac{72.1^2}{s^2 + 2(0.69)72.1s + 72.1^2}$$

Leading-edge flap:

$$\frac{47.22^2}{s^2 + 2(1.16)47.22s + 47.22^2}$$

Trailing-edge flap:

$$\frac{35^2}{s^2 + 2(1.42)35s + 35^2}$$

The QFT design consisted of 1) a yaw damper, 2) a $2 \times 2$ diagonal compensation matrix, and 3) two prefilters. These elements are defined as follows:

Yaw damper:

$$\frac{\delta_{\text{rud}}}{r}(s) = \frac{-9s}{s + 0.2}\ \frac{\text{rad}}{\text{rad/s}}$$

Note that this element was implemented downstream of the control distribution matrix **W**.

Compensation matrix:

$$\mathbf{G_c(s)} = \begin{bmatrix} G_p & 0 \\ 0 & G_\beta \end{bmatrix} = \begin{bmatrix} \frac{0.38(s+4.1)}{s} & 0 \\ 0 & \frac{130(s+1.1)(s+25)}{s(s+5)} \end{bmatrix}$$

Prefilters:

$$F_p(s) = \frac{4}{s+4}$$

and

$$F_\beta(s) = \frac{0.5}{s+0.5}$$

An aperiodic divergence exhibiting a large time-to-double amplitude was noted with this design. The instability was eliminated by creating a regulated variable $p_{\text{reg}} = p + 0.075\ r$.

## References


[1] Croft, J. W., "Refuse-to-Crash: NASA Tackles Loss of Control," *Aerospace America*, Vol. 41, No. 3, Mar. 2003, pp 42–45.

[2] Steinberg, M., "Historical Overview of Research in Reconfigurable Flight Control," *Proceedings of the Institution of Mechanical Engineers, Part G (Journal of Aerospace Engineering)*, Vol. 219, No. 4, 2005, pp. 263–276. doi:10.1243/095441005X30379

[3] Hess, R. A., and Wells, S. R., "Sliding Mode Control Applied to Reconfigurable Flight Control Design," *Journal of Guidance, Control, and Dynamics*, Vol. 26, No. 3, 2003, pp. 452–463. doi:10.2514/2.5083

[4] Wells, S. R., and Hess, R. A., "Multi-Input, Multi-Output Sliding Mode Control for a Tailless Fighter Aircraft," *Journal of Guidance, Control, and Dynamics*, Vol. 26, No. 3, 2003, pp. 463–473. doi:10.2514/2.5084

[5] Vetter, T. K., Wells, S. R., and Hess, R. A., "Designing for Damage—Robust Flight Control Design Using Sliding Mode Techniques," *Proceedings of the Institution of Mechanical Engineers, Part G (Journal of Aerospace Engineering)*, Vol. 217, No. 5, 2003, pp. 245–262. doi:10.1243/095441003770887359

[6] Hess, R. A., Vetter, T. K., and Wells, S. R., "Design and Evaluation of a Damage-Tolerant Flight Control System," *Proceedings of the Institution of Mechanical Engineers, Part G (Journal of Aerospace Engineering)*, Vol. 219, No. 4, 2005, pp. 341–360. doi:10.1243/095441005X7259

[7] Hess, R. A., and Ussery, T. M., "Frequency-Domain Sliding Mode Design Technique Applied to the Control of a Ducted-Fan Micro-Air Vehicle," *Journal of the American Helicopter Society*, Vol. 49, No. 4, 2004, pp. 457–467.

[8] Hess, R. A., and Bakhtiari-Nejad, M., "Sliding Mode Control of a Nonlinear, Ducted-Fan, UAV Model," *Journal of Guidance, Control, and Dynamics*, Vol. 31, No. 4, 2008, pp. 1163–1166. doi:10.2514/1.32558

[9] Hess, R. A., and Cama, G., "Frequency Domain, Pseudo Sliding Mode Control System for a Flexible Aircraft," *Proceedings of the Institution of Mechanical Engineers, Part G (Journal of Aerospace Engineering)*, Vol. 221, No. 5, 2007, pp. 707–717. doi:10.1243/09544100JAERO226

[10] Wells, S. R., "Application of Sliding Mode Methods to the Design of Reconfigurable Flight Control Systems," Ph.D. Dissertation, Dept. of Mechanical and Aeronautical Engineering, Univ. of California, Davis, Davis, CA, 2002.

[11] Hess, R. A., "Frequency-Domain Design/Analysis of Robust Flight Control Systems," *System Control Technologies, Design Considerations and Integrated Optimization Factors for Distributed Nano UAV Applications*, RTO-EN-SCI-175, NATO RTO Lecture Series, NATO Research and Technology Organization, Neuilly-sur-Seine, France, May 2007, pp. 3-1–3-55.

[12] Edwards, C., and Spurgeon, S. K., *Sliding Mode Control*, Taylor and Francis, London, 1998.

[13] Osman, C. L., "Design of Flight Control Laws for Aircraft with Flexible Wings Using Quantitative Feedback Theory," M.S. Thesis, AFIT/GE/ENG/95D-20, U.S. Air Force Inst. of Technology, Wright–Patterson AFB, OH, Dec. 1995, http://handle.dtic.mil/100.2/ADA309939.

[14] Maciejowski, J. N., *Multivariable Feedback Design*, Addison–Wesley, Wokingham, England, U.K., 1989, Chap. 1.

[15] Snell, S. A., "Decoupling Control Design with Application to Flight," *Journal of Guidance, Control, and Dynamics*, Vol. 21, No. 4, 1998, pp. 647–655. doi:10.2514/2.4284

[16] Hess, R. A., "Theory for Roll-Ratchet Phenomenon in High-Performance Aircraft," *Journal of Guidance, Control, and Dynamics*, Vol. 21, No. 1, 1998, pp. 101–108. doi:10.2514/2.4203

[17] Hess, R. A., "Unified Theory for Aircraft Handling Qualities and Adverse Aircraft-Pilot Coupling," *Journal of Guidance, Control, and Dynamics*, Vol. 20, No. 6, 1997, pp. 1141–1148. doi:10.2514/2.4169

[18] McRuer, D. T., and Krendel, E. S., "Mathematical Models of Human Pilot Behavior," AGARDograph 188, AGARD, Neuilly-sur-Seine, France, 1974.

[19] Mitchell, D. G., Aponso, B. L., and Klyde, D. H., "Effects of Cockpit Lateral Stick Characteristics on Handling Qualities and Pilot Dynamics," NASA CR-4443, June 1992.

[20] Hanlon, P. D., and Maybeck, P. S., "Interrelationship of Single-Filter and Multiple-Model Adaptive Algorithms," *IEEE Transactions on Aerospace and Electronic Systems*, Vol. 34, No. 3, 1998, pp. 934–946. doi:10.1109/7.705899

[21] Graham, D., and McRuer, D., *Analysis of Nonlinear Control Systems*, Dover, New York, 1971, Chap. 1.

[22] Houpis, C. H., Rasmussen, S. J., and Garcia-Sanz, M., *Quantitative Feedback Theory: Fundamentals and Applications*, 2nd ed., CRC Press, Boca Raton, FL, 2005.

[23] Anon., *Aviation Safety and Pilot Control—Understanding and Preventing Unfavorable Pilot-Vehicle Interactions*, National Academy Press, Washington, D.C., 1997, pp. 50–55.

[24] DeCarlo, R. A., Zak, S. H., and Drakunov, S. V., "Variable Structure, Sliding Mode Design," *The Control Handbook*, edited by W. S. Levine, CRC Press, Boca Raton, FL, 1996, pp. 941–951.

[25] Siwakosit, W., and Hess, R. A., "Multi-Input-Output Reconfigurable Flight Control Design," *Journal of Guidance, Control, and Dynamics*, Vol. 24, No. 6, 2001, pp. 1079–1088. doi:10.2514/2.4841

[26] Franklin, G. F., Powell, J. D., and Emami-Naeini, A., *Feedback Control of Dynamic Systems*, 4th ed., Prentice–Hall, Upper Saddle River, NJ, 2002, Chap. 8.